Journal of Nuclear Materials 403 (2010) 191–197

Contents lists available at ScienceDirect

Journal of Nuclear Materials

journal homepage: www.elsevier.com/locate/jnucmat

Processing effects on microstructure in Er and ErD_2 thin-films

Chad M. Parish *, Clark S. Snow, Daniel R. Kammler, Luke N. Brewer

Sandia National Laboratories, Albuquerque, NM, USA

ARTICLE INFO

Article history:
Received 5 February 2010
Accepted 12 June 2010

ABSTRACT

Erbium metal thin-films have been deposited on molybdenum-on-silicon substrates and then converted to erbium dideuteride (ErD_2). Here, we study the effects of deposition temperature (≈300 or 723 K) and deposition rate (1 or 20 nm/s) upon the initial Er metal microstructure and subsequent ErD_2 microstructure. We find that low deposition temperature and low deposition rate lead to small Er metal grain sizes, and high deposition temperature and deposition rate led to larger Er metal grain sizes, consistent with published models of metal thin-film growth. ErD_2 grain sizes are strongly influenced by the prior-metal grain size, with small metal grains leading to large ErD_2 grains. A novel sample preparation technique for electron backscatter diffraction of air-sensitive ErD_2 was developed, and allowed the quantitative measurement of ErD_2 grain size and crystallographic texture. Finer-grained ErD_2 showed a strong (1 1 1) fiber texture, whereas larger grained ErD_2 had only weak texture. We hypothesize that this inverse correlation may arise from improved hydrogen diffusion kinetics in the more defective fine-grained metal structure or due to improved nucleation in the textured large-grain Er.

1. Introduction

Long-term storage of the hydrogen isotopes deuterium (D) and tritium (T) is important for nuclear applications, such as compact neutron generators where D (or T) ions are accelerated into a thin metal film containing T (or D). Tritium radioactively decays with a half-life of 12.3 years into ^{3}He. Most of the ^{3}He in the metal tritide film accumulates into high-pressure helium bubbles while a small quantity, <1%, escapes from the film [1–3]. Helium bubbles can also be induced in metals by direct implantation of helium and via nuclear reactions [4]. In most cases, the formation, growth, and evolution of helium bubbles is impacted by the material's shear strength, surface energy [5], defects [6], dislocations [1,7,8], and grain boundaries [9–11]. Grain boundaries appear to play an important role when the helium concentration is high (>0.2 He/M) as the helium bubbles begin to decorate the grain boundary [12]. Further, the grain boundary may provide an easy path for helium atoms to percolate to the surface. What is particularly fascinating is that the initial metallic microstructure influences helium bubble evolution and when the helium bubbles reach a certain size and pressure they in turn induce changes in the host metallic microstructure [13,14]. This work will study the initial microstructure of erbium hydride films in preparation for a long-term and detailed study of how the microstructure influences and is changed by helium bubbles in metal tritides in general.

Long-term hydrogen storage is often accomplished through the reaction of the hydrogen isotope with a metal to produce a metal–hydride compound [15,16]. Important long-term hydrogen storage matrices are uranium and alloys [17–21], $LaNi_5$ and alloys [22–27], and erbium [28–35]. Recent reviews of the physics and chemistry of the metal–hydrogen system [36] and rare earths in particular [37] are available. Erbium dihydride $Er(H,D,T)_2$ is often produced in the form of polycrystalline thin-films on Mo metal or Mo/Si substrates [28–30,35]. These films are produced by electron-beam evaporating a layer of Er metal (100–1000 nm thick) onto a Mo substrate or evaporated-Mo interlayer, followed by hydrogen loading of the Er film into nominal $Er(H,D,T)_2$ stoichiometry.

Differences in processing will naturally lead to different microstructures in the final materials. This will, in turn, lead to differing final properties of the films. While the initial metal film microstructure can be manipulated by deposition rate and temperature, it is not clear how these differences in processing and in the resulting microstructures will manifest themselves in different metal hydride microstructures. In this work, we explore how grain sizes and crystallographic texture in ErD_2 thin-films grown on 100 nm Mo/(0 0 1) Si are affected by the substrate temperature and growth rate during the initial Er-metal deposition. As a part of this work, we also describe a novel technique to prepare easily-oxidized ErD_2 thin-films for electron backscatter diffraction.

* Corresponding author. Present address: Oak Ridge National Laboratory, Oak Ridge, TN, USA.
E-mail address: parishcm@ornl.gov (C.M. Parish).

0022-3115/$ - see front matter © 2010 Elsevier B.V. All rights reserved.
doi:10.1016/j.jnucmat.2010.06.026

2. Experiment

2.1. Film growth

Starting materials were 1 cm × 1 cm squares of silicon in the (0 0 1) orientation, approximately 500 μm thick. Mo was grown by electron-beam evaporation at 450 °C substrate temperature and 1 nm/s to thicknesses of 80–110 nm. Following the Mo deposition, Er metal was electron-beam evaporated to thicknesses of 500–550 nm. The Er evaporation occurred at low substrate temperature 25–35 °C, or at higher temperature, 450 °C. Evaporation rates were either 1 or 20 nm/s. Following metal deposition samples from each condition were combined together and loaded with deuterium to a nominal composition of $ErD_{2.0}$ in a single run. We summarize these conditions and provide nomenclature in Table 1.

A Si substrate was chosen to provide a very smooth final film, which is useful for additional studies such as ion-beam analysis. The Mo interlayer prevented the formation of erbium silicides. ~30 °C and 450 °C were chosen to put the thin-film growth within different regions of the structure-zone models (see Section 4.1.1), which allowed us to test hypotheses formed by applying the structure-zone models from the literature. ~500 nm film thickness was well adherent but previous work showed oxygen-pickup was not a major concern at ~500 nm as was seen in thinner films [35]. 1 nm/s and 20 nm/s bracketed the range of well-controllable and repeatable depositions with the equipment used.

2.2. Grain size and texture measurements

Transmission electron microscopy (TEM) samples were prepared in cross-section from the wafers using an FEI DB-235 dual-beam focused ion beam/scanning electron microscope (FIB/SEM) instrument. Milling was at 30 keV followed by 5 keV final polishing. Samples were lifted out and placed on carbon-filmed copper support grids. We obtained bright-field and dark-field TEM micrographs using a Phillips CM30 instrument at 300 keV.

Er metal grain sizes were measured by acquiring centered-dark-field cross-sectional TEM images. Grain areas were measured by marking the grains' perimeters using ImageJ software, and then converted to equivalent grain diameters.

We have shown FIB milling of ErD_2 films on silicon produced good quality foils for TEM analysis [28]. However, a FIB-cut TEM foil will typically be about 5 mm in extent, and we found this foil size to be of the same order as the hydride grain size of the present hydride samples, and thus these samples had insufficient sampling density to extract statistically useful data.

Electron backscatter diffraction (EBSD) in the SEM is a technique capable of measuring grain sizes and textures from large areas at high resolution, and is more appropriate for ErD_2 samples whose grain size is comparable to the size of a TEM foil. However, ErD_2 films are sensitive to air exposure and oxidize easily [28]. EBSD is also sensitive to surface state, and ErD_2 films examined by EBSD in plan view (electron beam striking the surface of the film) showed poor quality data, likely due to a thin near-surface oxide layer forming [28], thus preventing the formation of useable backscatter diffraction patterns. This data is therefore unsuitable for grain size or texture measurement. Standard metallographic cross-sectioning techniques could not be used due to the likely reaction of the film with water or solvents containing even small amounts of humidity. Thus, a dry vacuum-based sample preparation technique was needed.

Samples were prepared in cross-section by cleaving and ion-polishing. This is illustrated schematically in Fig. 1. First, the 1 cm × 1 cm silicon substrate (Fig. 1a) is cleaved. This cleaving typically yields cross-section faces with angles ~45° to the sample normal (Fig. 1b). If such angled faces are not obtained by cleaving, the sample can be beveled on 1200 grit sandpaper to this approximate angle. The cleaved half where the substrate slopes away from the film (i.e., left half, Fig. 1b) is then waxed onto a sample puck and inserted into a JEOL SM-09010 cross-sectional ion polisher. A sputter-resistant hard-mask is lowered over the edge of the sample as illustrated in Fig. 1c. An argon ion beam is then used to ion-mill the sample, leaving a large (~1–2 mm width) polished flat (Fig. 1d). Polishing conditions were typically 10 h at 5.0 keV, 90–110 mA, followed by 3 h at 2.5 keV, 15–25 mA. Polishing chamber base pressure was $\sim 5 \times 10^{-4}$ Pa, and operating pressure 2×10^{-3}–6×10^{-3} Pa. 2.5 keV finish polishing improved the EBSD hit rates compared to 5.0 keV finish polishing.

Samples were then removed from the polisher vacuum and inserted into the SEM chamber. After air exposures ~2–10 min, the hydride samples still provided acceptable indexing percentages (~50%) in EBSD. However, storage of these samples in air for more than about 1 h resulted in a total loss of EBSD patterns from the film. As such, all EBSD data presented in this work were obtained on samples transferred immediately from the polishing chamber to the SEM chamber. EBSD was performed in a Zeiss Supra VP55 field emission SEM equipped with an HKL Technologies Channel 5 EBSD system. Beam voltage was 20 keV and step sizes were 50 or 100 nm, with 20 ms integration averaged 5–10×. Fig. 2 shows a typical SEM cross-section with the sample EBSD coordinate system marked. Hydride grain sizes were measured as the in-plane width at one-half of the film thickness. Because EBSD is a rastered, serially-acquired technique, sample drift is unavoidable at the

Table 1
Sample matrix and nomenclature.

Deposition temperature	Deposition rate	Material	Designation
25–35 °C (Low)	1 nm/sec (Slow)	Er metal	Metal/Low/Slow
		ErD_2	Hydride/Low/Slow
	20 nm/sec (Fast)	Er metal	Metal/Low/Fast
		ErD_2	Hydride/Low/Fast
450 °C (High)	1 nm/sec (Slow)	Er metal	Metal/High/Slow
		ErD_2	Hydride/High/Slow
	20 nm/sec (Fast)	Er metal	Metal/High/Fast
		ErD_2	Hydride/High/Fast

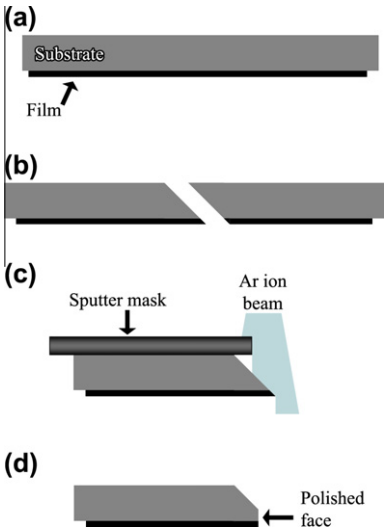

Fig. 1. Schematic of sample preparation procedure. (a) Starting sample is turned upside down. (b) Sample is cleaved, yielding inclined faces along the cross-section. (c) Sample is ion-polished, yielding. (d) A smooth, clean film cross-section for EBSD measurements. Figure is not to scale; samples are ~10 mm wide and ~0.5 mm thick, and the film is $\sim 5 \times 10^{-4}$ mm thick.

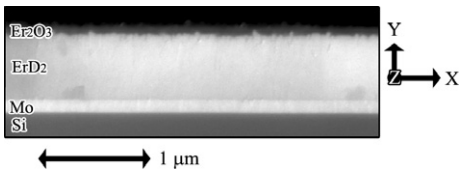

Fig. 2. An in-lens-detector SEM cross-section shown along with the sample coordinate system, sample Hydride/Low/Slow.

long dwell-times and fine pixel spacing necessary to examine small, defective grains like ErD_2. The fast-scan directions of the EBSD maps were in the plane of the film, so sample drift, when present, will not appreciably distort measurements in that scan direction. However, due to drift, grain areas and thus equivalent diameters could not always be measured, as was the case for the Er metal.

Texture measurements were also performed via X-ray diffraction. XRD data were collected on a Bruker D8 Discover diffractometer equipped with an Eulerian cradle, Goebel mirrors on both primary and diffracted beam sides, a Cu X-ray source, and a scintillation detector. In order to obtain texture information from the Er-metal samples data was collected over a range of Chi (χ), Phi (ϕ) and 2θ. A 1 mm pinhole snout was placed after the primary beam Goebel mirror and a 0.6 mm fixed width receiving slit was placed between the Goebel mirror and the scintillation detector on the diffracted beam side. χ was advanced in 6° increments from 0° to 72°. At each position of χ, ϕ was advanced in 6° increments between 0° and 354°. $\theta/2\theta$ scans between 28.5° and 34.46° in 2θ (0.04° step size and 1 s count time) were then collected at each combination of χ and ϕ. Pole figures for the Er (1 0 0), (0 0 2), and (1 0 1) peaks were then extracted from these data sets for each Er-metal sample. For the ErD_2 samples $\theta/2\theta$ scans were collected between 20 and 80° in 2θ with a 0.04° step size and 1 s count time. Fixed width 0.6 mm slits were used on both primary and diffracted beam sides for the $\theta/2\theta$ scans. In some cases the $\theta/2\theta$ scans for the ErD_2 samples had to be repeated at $\chi = 3°$ to limit the intensity of the Si (4 0 0) substrate peak which was very intense. X-ray diffraction of ErD_2 samples did not show the presence of Er or ErD_3, indicating the hydride films were in the single phase region, approximately $ErD_{2.0}$–$ErD_{2.1}$ [38].

3. Results

3.1. Er-metal films

Fig. 3 shows representative bright-field TEM data from the four Er-metal samples. The Metal/Low samples (top row) show narrow, columnar grains, ~20 nm in diameter, but not extending through the full ~500 nm film thickness. The Metal/High samples (second row) show much wider grains, several hundred nanometers in

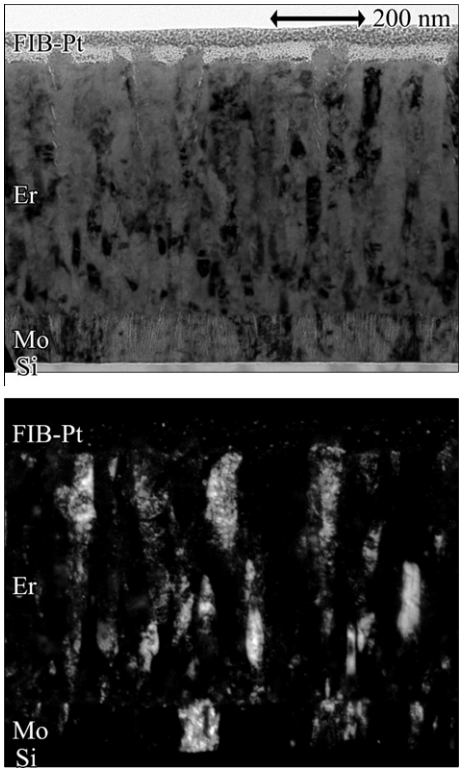

Fig. 4. Representative bright-field/dark-field image pair of the Metal/Low/Slow sample, illustrating the grain size measurements.

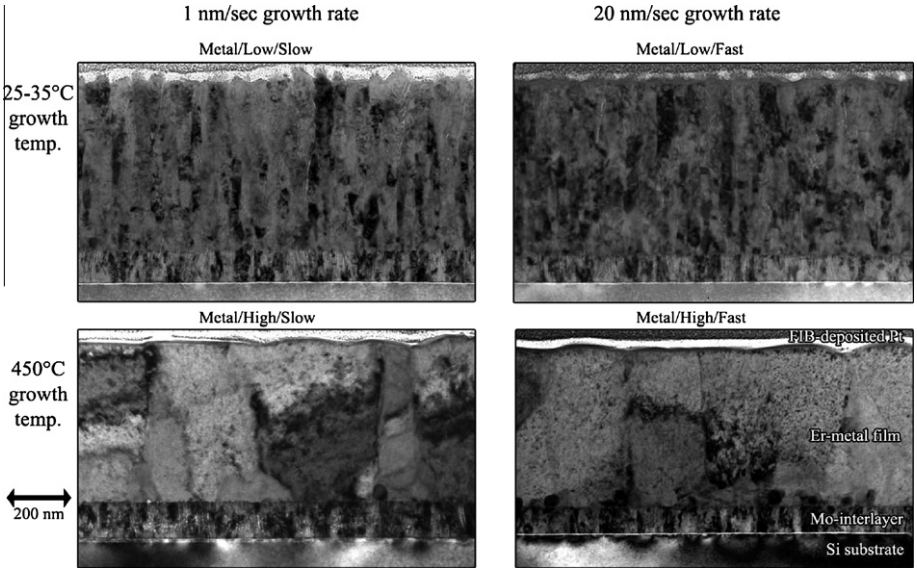

Fig. 3. Representative bright-field TEM micrographs of the four Er-metal samples. Speckled contrast is likely a Ga-FIB artifact.

diameter, which are columnar and extend through the film thickness. A bright-field/dark-field image pair of sample Metal/Low/Slow is shown in Fig. 4. Table 2 gives grain diameter measurements for the four samples. The Metal/Low (25–35 °C) samples' grain diameters are significantly smaller than the Metal/High (450 °C) grain sizes. The 20 nm/s samples appear to have slightly larger grain sizes than the 1 nm/s samples, but this difference is minor.

X-ray texture data indicated that the Metal/Low samples had random textures, and the Metal/High samples had mixed (1 0 1) and (0 0 2) fiber textures. The Er-metal samples did not provide usable EBSD signals. EBSD is limited to grain sizes on the order of 50–200 nm and larger, depending on the sample material, microscope resolution, and operating conditions. Therefore it was necessary to use TEM to measure the Er metal grain sizes and XRD to measure the texture.

3.2. ErD_2 films

Fig. 5 shows typical *Z*-direction inverse pole figure (IPF) maps from the four hydride samples. The first observation is that the grains are columnar, so grain sizes in the growth direction are the film thickness, 500–600 nm. The raw EBSD maps show 20+% non-indexable (black) pixels in the film. Noise-reduction was performed on the data in Fig. 5, filling in these isolated black pixels with data calculated from the surrounding pixels using 5-nearest-neighbor algorithm in HKL's Tango software, in order to better differentiate the grain boundary locations.

Grain width results for the ErD_2 films are summarized in Table 3. These results indicate that the low-deposition-temperature samples showed significantly larger average grain widths than the high-deposition-temperature samples. At either temperature, the fast-deposition-rate samples had slightly larger average grain sizes than the low-deposition-rate samples. Grain widths in any sample are highly variable, resulting in the large standard deviations.

The Hydride/High/Slow sample's grain width was also measured via TEM and was comparable to the results from EBSD. The grain width was 0.7 ± 0.4 μm via TEM and 0.9 ± 0.5 μm via EBSD. Due to the large hydride grain sizes, TEM was again not an ideal technique for these measurements. However, this result indicates that TEM and EBSD measured grains sizes can be reasonably compared.

Fig. 6 shows the *Y*-direction IPF maps for Hydride/Low/Slow and Hydride/High/Slow. The Hydride/High/Slow (Fig. 6b) and Hydride/High/Fast samples (not shown) indicate strong (1 1 1) fiber textures with respect to the deposition direction. The Hydride/Low/Slow (Fig. 6a) and Hydride/Low/Fast samples (not shown) did not indicate particularly strong textures. Pole figure calculations quantitatively confirm these qualitative results. The pole figures for the Hydride/High/Slow sample are shown in Fig. 6c. The pole figure shows a strong (1 1 1) peak (>8× random) very near the *Y*-(growth) direction. The slight deviation from exact (1 1 1) || growth direction is likely due to a slight misalignment of the sample with respect to the SEM chamber coordinate system. Because EBSD texture measurements are based on small numbers of grains, it is pos-

Table 2
Er grain sizes. ⟨*D*⟩, mean grain diameter; *s*(*D*), grain diameter standard deviation. *N*, the number of grains contributing to the measurement.

	Equivalent diameter ⟨*D*⟩ ± *s*(*D*) (μm)	Number, *N*
Metal/Low/Slow	0.12 ± 0.03	40
Metal/Low/Fast	0.15 ± 0.04	69
Metal/High/Slow	0.33 ± 0.09	28
Metal/High/Fast	0.34 ± 0.10	38

Table 3
ErD_2 grain sizes. ⟨*W*⟩, mean grain width; *s*(*W*), grain width standard deviation. *N*, the number of grains contributing to the measurement.

	Grain width ⟨*W*⟩ ± *s*(*W*)	Number, *N*
Hydride/Low/Slow	3.0 ± 2.4	52
Hydride/Low/Fast	3.2 ± 3.0	67
Hydride/High/Slow	0.9 ± 0.5	32
Hydride/High/Fast	1.7 ± 1.2	17

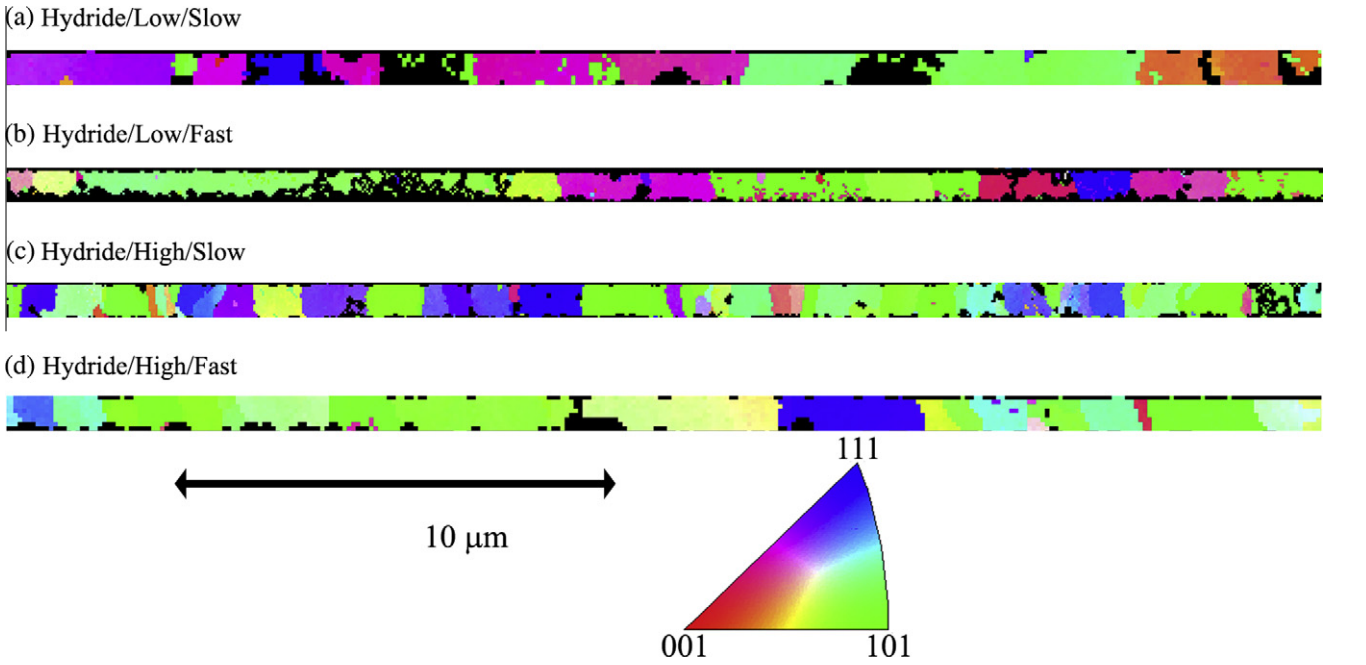

Fig. 5. *Z*-axis IPF maps of the hydride samples prepared by ion-cross-sectioning. Note the small and large grains in each sample; this causes the large standard deviations in grain size measurements.

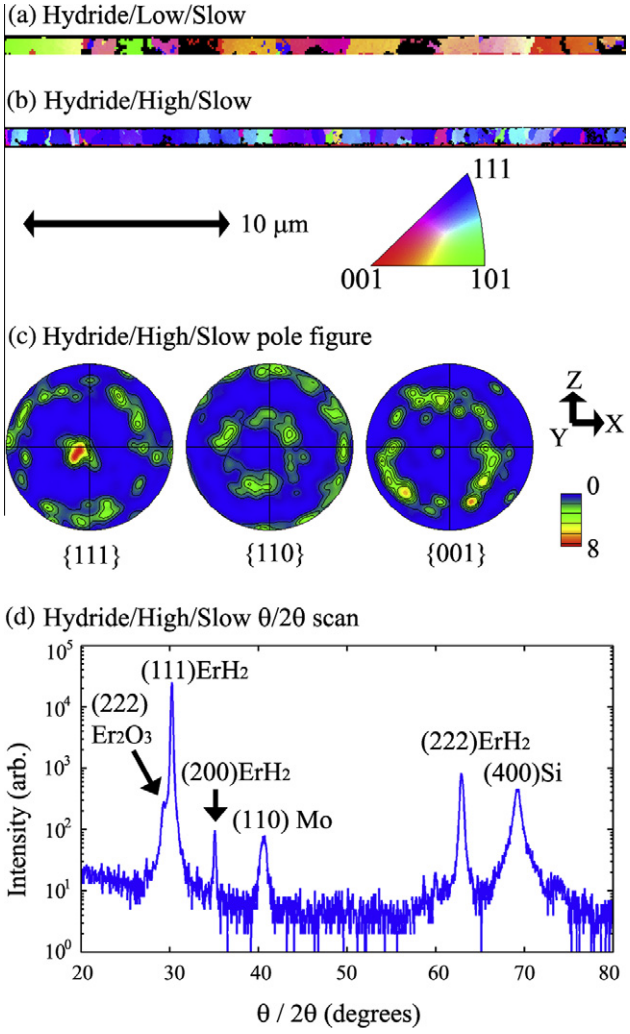

Fig. 6. (a) Hydride/Low/Slow. (b) Hydride/High/Slow Y-direction IPF maps. (c) Hydride/High/Slow pole figures. (d) Hydride/High/Slow $\theta/2\theta$ scan; note strong (1 1 1) hydride signal.

sible for a particularly large grain to bias texture calculations. X-ray diffraction was used to verify the EBSD texture measurements. The $\theta/2\theta$ XRD pattern collected from the Hydride/Low/Slow sample appeared similar to a calculated random texture pattern. The $\theta/2\theta$ XRD pattern collected from the Hydride/Low/Fast sample showed a weak (0 0 2) out-of-plane texture. These results are consistent with the EBSD results. $\theta/2\theta$ XRD patterns collected from the Hydride/High/Slow (Fig. 6d) and Hydride/High/Fast samples showed very sharp (1 1 1) out-of-plane textures. These results are also consistent with the EBSD data.

4. Discussion

4.1. Er-metal films

4.1.1. Expected behavior

The effect of growth parameters on deposited thick- and thin-film microstructures has been discussed and reviewed by many authors [39–43]; the seminal paper for metal thin-films was that of Grovenor et al. [44], and the specific case of Er-thin-films was studied by Savaloni et al. [45,46] and Gu et al. [47]. These references suggest structure-zone models (SZMs), in which the structure of the polycrystalline thin-film is determined by processing parameters, primarily the homologous substrate temperature during deposition, defined as T_S/T_M, where T_S is the substrate temperature in kelvins and T_M the melting point of the film material in kelvins.

The SZMs suggest four general regions of T_S/T_M behavior. At low T_S/T_M, typically $T_S/T_M < 0.2$, "Zone 1" behavior manifests. This regime shows small grains, typically a few 10–100 s of nanometers in size. This results from a high nucleation rate for grains but limited adatom mobility. Individual grains may be separated by pores or voids. Columnar grains [41] and equiaxed grains [44] have been described for this regime. A strongly preferred orientation is not expected [43]. At slightly higher T_S/T_M, typically 0.3–0.5, "Zone 2" behavior manifests. Here, bulk diffusion begins, and a clear columnar structure is observed, with grain diameters typically less than the film thickness. The grain boundaries do not show pores or voids. A preferred orientation, such as ⟨0 0 2⟩-axis orientation in hexagonal materials like Er, will also be expected [43]. Between Zone 1 and Zone 2 exists "Zone T" (for "transition"), with approximate T_S/T_M 0.2–0.3, where the structure is intermediate between the Zone 1 and Zone 2 behavior. This zone is defined by adatom surface mobility but very limited bulk diffusivity. "Zone 3" behavior begins at higher T_S/T_M, typically >0.5, where large numbers of grain boundaries are mobile and grain growth will be pronounced, leading to larger grain structures, often with abnormal grain growth.

Growth rate effects, in addition to substrate temperature effects, have also been noted. For Er-metal films, it was found that for higher T_S a higher growth rate lead to larger grain sizes in many cases [45].

4.1.2. Comparison to experiment

Our Er-metal results (Section 3.1) are generally consistent with these structure-zone models. The Metal/Low samples were grown at ~25–35 °C (~300 K). The melting point of Er is 1529 °C (1802 K), so $T_S/T_M \approx 0.17$. For the Metal/High samples, the growth temperature was 450 °C (723 K), so $T_S/T_M \approx 0.40$. This would imply upper Zone 1 behavior for the Metal/Low samples, and middle Zone 2 behavior for the Metal/High samples.

The Metal/Low samples showed roughly columnar grains with small equivalent diameters ~100–200 nm, and a few tens of nanometers in column width. This is consistent with Zone 1 to borderline Zone T behavior and is expected from the high nucleation rate and very limited surface mobility of adatoms at ~300 K. Grain heights were typically less than the thickness of the film, indicating renucleation over the course of growth. Previous work has attributed this behavior to imperfect vacuum resulting in segregated impurities [39,45,46,48].

The Metal/High samples showed mostly columnar grains with equivalent diameters ~300 nm. This is consistent with the higher adatom mobility associated with the 723 K growth temperature. Further, the Metal/High/Fast sample did show slightly larger grain sizes than the Metal/High/Slow sample, which is consistent with previous deposition-rate results. Texture measurements showed a (1 0 1) and (0 0 2) fiber texture in the 450 °C samples, also consistent with the Zone 2 SZMs.

4.2. ErD_2 films

While the Er-metal behavior follows standard models, the ErD_2 behavior is more puzzling. As seen in Table 3, the Hydride/Low samples have larger grain sizes than the Hydride/High samples. As seen in Table 2, the Metal/Low samples have significantly smaller grain sizes than the Metal/High samples. Thus, the hydride films grown from fine-grained metal show significantly larger hydride grain sizes than films grown from larger-grained metal films. Fig. 7 shows this inverse relationship in grain sizes. It is a very

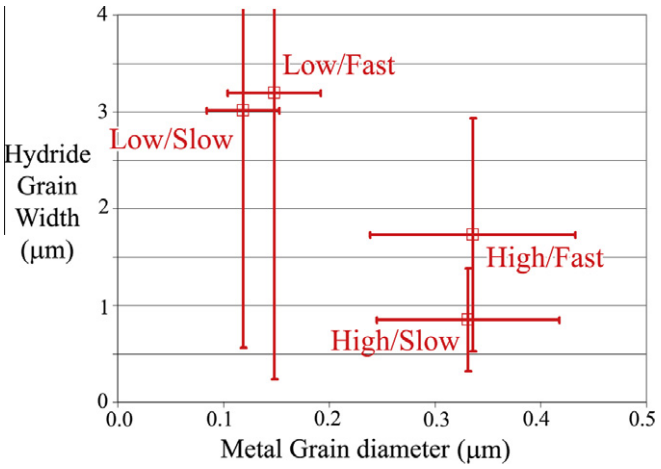

Fig. 7. Hydride grain widths as a function of prior-metal grain diameters. Note 8× difference in scale between ordinate and abscissa.

interesting question why large prior-metal grains should result in small hydride grains, and vice versa. We summarize the structural evolution in Fig. 8.

Although we cannot yet confirm what atomistic process is responsible for this result, we can present hypothetical models for future experimental testing. When phase or grain growth is favored in comparison to nucleation, grain sizes tend to be larger than when phase nucleation is favored over growth. The Hydride/Low samples appear to show that growth is favored over nucleation in comparison to the Hydride/High samples. Because the Metal/Low samples have larger densities of grain boundaries, voids, and other defects, it is possible that these defects are acting as high-diffusivity paths and allow faster transport of deuterium for enhanced growth rates. Future studies involving interrupted transformations at different times may help elucidate the microscopic behavior leading to these observations and confirm or refute this hypothetical model.

It is also interesting to note that the metal samples which showed random texture (Low/Slow and Low/Fast) also showed no or only weak crystallographic texture in hydride form, and that the metal samples that showed fiber textures also showed fiber texture in hydride form. These texture results suggest that the hydride nuclei inherit their texture from the prior-Er grains' texture. Because the prior-Er texture was a mixed ⟨1 0 1⟩ and ⟨0 0 2⟩ fiber, but the ErD_2 showed a single ⟨1 1 1⟩ fiber, this may also indicate that metal grains with one texture or the other are more favorable for heterogeneous nucleation of hydride grains. Because the (0 0 2) Er and (1 1 1) ErD_2 planes are close-packed, the texture selection is probably (1 1 1) ErD_2 templating off (0 0 2) Er; this inference is likely but not proven at present. This texture selection could imply easier nucleation which could contribute to the smaller grain size of the textured hydrides, in addition to the previously mentioned possibility of faster hydrogen diffusion and growth in the large-grained hydrides. Additionally, Gu et al. [47] noted that under certain conditions, the earliest stages of Er-metal growth would proceed as FCC-ErH_2. Hypothetically, if such a situation obtained in the Metal/High samples but not Metal/Low samples, and this small volume fraction of hydride persisted through metal growth to the beginning of deuterium loading, this pre-existing hydride volume fraction might serve as ready-made nucleation sites for ErD_2. In our work, if the smaller hydride grain sizes at Hydride/High conditions were due to increased presence of pre-existing hydride nuclei in Metal/High samples, this would imply more hydride contamination at higher metal growth temperature than at lower growth temperature. Gu et al. saw hydride (via X-ray diffraction methods) at low substrate temperature, and saw oxide rather than hydride in early stages of metal growth at higher temperature. This is somewhat inconsistent with the present results, where attribution of the inverse grain size relation to pre-existing hydride would require invocation of more pre-existing hydride at higher-temperature growth. However, very different substrates, preparation methods, and vacuum practices were used between the study of Gu et al. and the current study; further, Gu et al. noted that at higher temperatures substrate influences become more important [47]. Thus, it not possible to directly compare the previous results to the present results. If the above-proposed interrupted-growth experiments indicate hydride nucleation at the substrate, rather than some other location, the possibility of pre-existing hydride in the metal starting structure would need to be explored in more depth. Cross-sectional energy-filtered TEM plasmon-loss spectrum imaging in a monochromated instrument with a high-resolution energy filter would likely be an effective means to image such pre-existing hydride nuclei, if present. It is not possible at present to judge the relative possibilities of enhanced growth kinetics hypothesis vs. pre-existing nuclei hypothesis.

Unlike growth of metal thin-films (Section 4.1.1), there is little literature to guide us in understanding the mechanisms for conversion of a metallic thin-film into a hydride thin-film. The primarily studied example system is Pd-capped Mg/MgH_2, but most studies in this system emphasize kinetic effects of hydrogen unloading, rather than microstructural evolution during hydrogen loading. Kelekar et al. noted that textured polycrystal Mg transformed to MgH_2 faster than epitaxial single-crystal Mg [49], although this could not be definitively attributed to faster hydrogen diffusion in the polycrystal Mg, which we hypothesize to be present in our finer-grained Er materials. It has also been noted that textured Mg can result in textured MgH_2 [49,50], which seems to also be the case in our Er → ErD_2 transformations. Work on uranium hydride [51] has also found the hydriding kinetics and hydride structure to be very sensitive to the starting metallurgical structure.

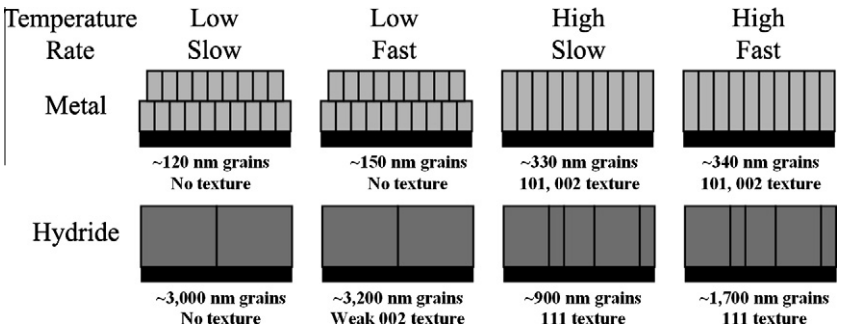

Fig. 8. Schematic summary of the observed microstructural evolution through processing.

5. Conclusions

Er-metal thin-films were deposited on Mo/Si substrates at high and low substrate temperature at fast and slow deposition rates. Higher substrate temperatures and faster deposition rates correlated with larger grain sizes. The results are consistent with published structure-zone models for thin-film Er-metal deposition.

Deposited metal films converted to ErD_2 showed significant differences in hydride grain size depending on the prior metal structure. Counterintuitively, smaller metal grain sizes correlated to larger hydride grain sizes and vice versa, possibly due to improved hydride growth kinetics in the highly defective finer-grained metal starting structures or due to easier hydride nucleation in the textured metal. Strong (1 1 1) fiber textures were observed in finer-grained hydride samples.

Finally, we described a dry, ion-based preparation method for making cross-sectional SEM/EBSD samples of the air-sensitive hydride films. We obtained good results from carefully prepared samples, despite the strong tendency to form oxidized surfaces that interfere with Kikuchi-pattern formation in EBSD.

Acknowledgements

Sandia is a multiprogram laboratory operated by Sandia Corporation, a Lockheed Martin Company, for the United States Department of Energy's National Nuclear Security Administration under contract DE-AC04-94AL85000. Liz Holm, Bonnie McKenzie, and Joseph Michael provided valuable technical advice and assistance. Ryan Wixom (SNL), Rob Ferrizz (SNL), Ed Kenik (ORNL) and Ray Unocic (ORNL) critiqued the manuscript. Thanks to Dale Zschiesche for collecting the XRD data.

References

[1] T. Schober, H. Trinkaus, R. Lasser, Journal of Nuclear Materials 141 (1986) 453–457.
[2] G.J. Thomas, Radiation Effects and Defects in Solids 78 (1–4) (1983) 37–51.
[3] L.C. Beavis, W.J. Kass, Journal of Vacuum Science & Technology 14 (1) (1977) 509–513.
[4] R. Blackburn, Inert Gasses in Metals, Metallurgical Reviews 11 (1966) 159–176.
[5] D.F. Cowgill, Helium Nano-bubble evolution in aging metal tritides, 2004.
[6] T. Schober, H. Trinkaus, Zeitschrift Fur Physikalische Chemie-International Journal of Research in Physical Chemistry & Chemical Physics 183 (1994) 473–477.
[7] T. Schober, H. Trinkaus, ^{3}He effects in tritides, in: S.E. Donnelly, J.H. Evans (Eds.), Fundamental Aspects of Intert Gases in Solids, Plenum, New York, 1991.
[8] M.P. Surh, J.B. Sturgeon, W.G. Wolfer, Radiation swelling behavior and its dependence on temperature, dose rate and dislocation structure evolution. Journal of Nuclear Materials 341(2–3) (2005) 235–236.
[9] H. Trinkaus, B.N. Singh, M. Victoria, Journal of Nuclear Materials 233 (1996) 1089–1095.
[10] H. Trinkaus, B.N. Singh, Journal of Nuclear Materials 323 (2–3) (2003) 229–242.
[11] J. Chen, P. Jung, H. Trinkaus, Physical Review B 61 (19) (2000) 12923–12932.
[12] G.M. Bond, J.F. Browning, C.S. Snow, Journal of Applied Physics 107 (8) (2010) 083514.
[13] Z. Xiaosong, L. Xinggui, Z. Lin, P. Shuming, L. Shunzhong, Journal of Nuclear Materials 396 (2010) 223–227.
[14] M.A. Rodriguez, J.F. Browning, C.S. Frazer, C.S. Snow, R.G. Tissot, E.P. Boespflug, Powder Diffraction 22 (2) (2007) 118–121.
[15] B. Sakintuna, F. Lamari-Darkrim, M. Hirscher, International Journal of Hydrogen Energy 32 (9) (2007) 1121–1140.
[16] J.P. Blackledge, An introduction to the nature and technology of hydrides, in: W.M. Mueller, J.P. Blackledge, G.G. Libowitz (Eds.), Metal Hydrides, Academic Press, New York, 1968, pp. 2–21.
[17] R.E. Rundle, Journal of the American Chemical Society 73 (9) (1951) 4172–4174.
[18] R.N.R. Mulford, F.H. Ellinger, W.H. Zachariasen, Journal of the American Chemical Society 76 (1) (1954) 297–298.
[19] T.B. Scott, G.C. Allen, I. Findlay, J. Glascott, Philosophical Magazine 87 (2) (2007) 177–187.
[20] G.G. Libowitz, The actinide hydrides, in: W.M. Mueller, J.P. Blackledge, G.G. Libowitz (Eds.), Metal Hydrides, Academic Press, New York, 1968, pp. 386–440.
[21] K.A. Terrani, G.W. Chinthaka Silva, C.B. Yeamans, M. Balooch, D.R. Olander, Journal of Nuclear Materials 392 (2009) 151–157.
[22] K.L. Shanahan, J.S. Holder, D.R. Bell, J.R. Wermer, Journal of Alloys and Compounds 356 (2003) 382–385.
[23] B.Y. Ao, S.X. Chen, G.Q. Jiang, Journal of Alloys and Compounds 390 (1–2) (2005) 122–126.
[24] K. Sakaki, Y. Nakamura, Y. Shirai, R.C. Bowman, E. Akiba, Materials Transactions 47 (8) (2006) 1875–1877.
[25] F.A. Kuijpers, H.H. van Mal, Journal of the Less-common Metals 23 (4) (1971). 395-&.
[26] H.H. van Mal, K.H.J. Buschow, A.R. Miedema, Journal of the Less-common Metals 35 (1) (1974) 65–76.
[27] A. Nobile, R.T. Walters, W.C. Mosley, Journal of the Less-common Metals 172 (1991) 1352–1362.
[28] C.M. Parish, C.S. Snow, L.N. Brewer, Journal of Materials Research 24 (5) (2009) 1868–1879.
[29] C.R. Tewell, S.H. King, Applied Surface Science 253 (2006) 2597–2602.
[30] J.A. Knapp, J.F. Browning, Journal of Nuclear Materials 350 (2) (2006) 147–152.
[31] J.R. Brangan, S.M. Thornberg, M.R. Keenan, Journal of Vacuum Science & Technology A – Vacuum Surfaces and Films 17 (4) (1999) 125–2131.
[32] J.A. Grimshaw, F.J. Spooner, C.G. Wilson, A.D. McQuillan, Journal of Materials Science 16 (10) (1981) 2855–2859.
[33] E.J. Fernandez, D.M. Holloway, Journal of Vacuum Science & Technology 11 (3) (1974) 612–613.
[34] W.M. Mueller, The rare-earth hydrides, in: W.M. Mueller, J.P. Blackledge, G.G. Libowitz (Eds.), Metal Hydrides, Academic Press, New York, 1968, pp. 386–440.
[35] C.S. Snow, L.N. Brewer, D.S. Gelles, M.A. Rodriguez, P.G. Kotula, M.A. Mangan, J.F. Browning, Journal of Nuclear Materials 374 (2008) 147–157.
[36] Y. Fukai, The Metal–Hydrogen System, Spring, Berlin, 2005.
[37] P. Vajda, Hydrogen in rare-earth metals, including RH_{2+x} phases, in: K.A. Gschneidner, L. Eyring (Eds.), Handbook on the Physics and Chemistry of Rare Earths, vol. 20, Elsevier, Amsterdam, 1995, pp. 207–291.
[38] A. Boukraa, P. Vajda, J.N. Daou, Journal of Magnetism and Magnetic Materials 123 (1–2) (1993) P.L5–L8.
[39] P.B. Barna, M. Adamik, Thin Solid Films 317 (1998) 27–33.
[40] N. Kaiser, Applied Optics 41 (16) (2002) 3053–3060.
[41] M. Ohring, Materials Science of Thin Films Deposition and Structure, Academic Press, San Diego, 2002.
[42] J.A. Thornton, Annual Review of Materials Science 7 (1977) 239–260.
[43] I. Petrov, P.B. Barna, L. Hultman, J.E. Greene, Journal of Vacuum Science & Technology A – Vacuum Surfaces and Films 21 (5) (2003) S117–S128.
[44] C.R.M. Grovenor, H.T.G. Hentzell, D.A. Smith, Acta Metallurgica 32 (5) (1984) 773–781.
[45] H. Savaloni, M.A. Player, Vacuum 46 (2) (1995) 167–179.
[46] H. Savaloni, M.A. Player, E. Gu, G.V. Marr, Vacuum 43 (10) (1992) 965–980.
[47] E.D. Gu, H. Savaloni, M.A. Player, G.V. Marr, Journal of Physics and Chemistry of Solids 53 (1) (1992) 127–136.
[48] P.B. Barna, M. Adamik, Formation and characterization of the structure of surface coatings, in: Y. Pauleau, P.B. Barna (Eds.), Protective Coatings and Thin Films, Kluwer Academic, Dordrecht, 1997, pp. 279–297.
[49] R. Kelekar, H. Giffard, S.T. Kelly, B.M. Clemens, Journal of Applied Physics 101 (11) (2007) 114311.
[50] A. Leon, E.J. Knystautas, J. Huot, R. Schulz, Journal of Alloys and Compounds 345 (1–2) (2002) 158–166.
[51] J. Bloch, M.H. Mintz, The Kinetics of Hydride Formation in Uranium, IAEC Annual Report 2001. <http://www.iaec.gov.il/docs/IAEC15.pdf>.